Icarus **148**, 437–455 (2000)
doi:10.1006/icar.2000.6503, available online at http://www.idealibrary.com on IDEAL®

High-Resolution Thermal Inertia Mapping from the Mars Global Surveyor Thermal Emission Spectrometer

Michael T. Mellon

Laboratory for Atmospheric and Space Physics, University of Colorado, Boulder, Colorado 80309
E-mail: mellon@argyre.colorado.edu

Bruce M. Jakosky

Laboratory for Atmospheric and Space Physics and Department of Geological Sciences, University of Colorado, Boulder, Colorado 80309

Hugh H. Kieffer

U.S. Geological Survey, Flagstaff, Arizona 86001

and

Philip R. Christensen

Department of Geology, Arizona State University, Tempe, Arizona 85287

Received January 17, 2000; revised July 21, 2000

High-resolution thermal inertia mapping results are presented, derived from Mars Global Surveyor (MGS) Thermal Emission Spectrometer (TES) observations of the surface temperature of Mars obtained during the early portion of the MGS mapping mission. Thermal inertia is the key property controlling the diurnal surface temperature variations, and is dependent on the physical character of the top few centimeters of the surface. It represents a complex combination of particle size, rock abundance, exposures of bedrock, and degree of induration. In this work we describe the derivation of thermal inertia from TES data, present global scale analysis, and place these results into context with earlier work. A global map of nighttime thermal-bolometer-based thermal inertia is presented at $\frac{1}{4}^\circ$ per pixel resolution, with approximately 63% coverage between 50°S and 70°N latitude. Global analysis shows a similar pattern of high and low thermal inertia as seen in previous Viking low-resolution mapping. Significantly more detail is present in the high-resolution TES thermal inertia. This detail represents horizontal small-scale variability in the nature of the surface. Correlation with albedo indicates the presence of a previously undiscovered surface unit of moderate-to-high thermal inertia and intermediate albedo. This new unit has a modal peak thermal inertia of 180–250 J m^{-2} K^{-1} s$^{-\frac{1}{2}}$ and a narrow range of albedo near 0.24. The unit, covering a significant fraction of the surface, typically surrounds the low thermal inertia regions and may comprise a deposit of indurated fine material. Local 3-km-resolution maps are also presented as examples of eolian, fluvial, and volcanic geology. Some impact crater rims and intracrater dunes show higher thermal inertias than the surrounding terrain; thermal inertia of aeolian deposits such as intracrater dunes may be related to average particle size. Outflow channels and valleys consistently show higher thermal inertias than the surrounding terrain. Generally, correlations between spatial variations in thermal inertia and geologic features suggest a relationship between the hundred-meter-scale morphology and the centimeter-scale surface layer.

INTRODUCTION

The Thermal Emission Spectrometer (TES) onboard the Mars Global Surveyor spacecraft (MGS) has obtained high spatial resolution (approximately 3 km) temperature observations of the martian surface. Diurnal cycles in the surface temperature are strongly dependent on the thermal and physical properties of the top several centimeters of the "soil." Many factors have an effect on temperature including albedo, dust opacity, and atmospheric pressure, but thermal inertia is the key property in controlling these temperature oscillations. Thermal inertia is defined as a combination of thermal conductivity k, density ρ, and heat capacity c:

$$I \equiv \sqrt{k\rho c}. \tag{1}$$

It represents the ability of the subsurface to conduct and store heat energy away from the surface during the day and to return that heat energy to the surface through the night. Deriving and understanding the thermal inertia of a surface can help to identify the small-scale characteristics of that surface. Fine grained and loosely packed material typically exhibits a low value of

0019-1035/00 $35.00

thermal inertia, while higher values are common for rocks and exposed bedrock. The thermal inertia of a region of the martian surface is generally related to properties such as particle size, degree of induration, abundance of rocks, and exposure of bedrock, including combinations of these properties within the field of view. Therefore, both global and local mapping of thermal inertia provides insight into the physical character of the martian surface and the geologic processes that have formed and modified that surface. We use TES observations of surface temperature to derive and map the thermal inertia of the martian surface layer.

Previous efforts to determine the thermal inertia of the martian surface worked from telescopic and spacecraft observations of brightness temperature. For example, Sinton and Strong (1960) conducted Earth-based limb-to-limb scans to estimate the diurnal variations in surface temperature and derived a thermal inertia of 170 (given throughout in units of J m^{-2} K^{-1} $s^{-\frac{1}{2}}$) to match the diurnal phase and 420 to match the amplitude. (To convert to the historical 10^{-3} cal cm^{-2} K^{-1} $s^{-\frac{1}{2}}$ units, divide by a factor of 41.86.) Leovy (1966) and Morrison *et al.* (1969) reanalyzed the data of Sinton and Strong, incorporating atmospheric effects on the surface temperature. Moroz and Ksanfomaliti (1972) and Moroz *et al.* (1976) used Mars-3 orbit tracks to estimate the thermal inertia for various light and dark regions over the surface. Ksanfomaliti and Moroz (1975) conducted a similar study from Mars-5 data. Neugebauer *et al.* (1971) use Mariner 6 and 7 flyby data to derive a global estimate and values for Hellas and Isidis. Kieffer *et al.* (1973) derived a global average thermal inertia of 290 from Mariner 9 data and regional extremes of 210 South Tharsis and 500 for Hellas.

Kieffer *et al.* (1977) reported a preliminary map of thermal inertia at a resolution of 2° in longitude and latitude from Viking IRTM (Infrared Thermal Mapper) data. They found a range of thermal inertias from about 70 to 500 and a strong bimodal anticorrelation with albedo. Palluconi and Kieffer (1981) reported what has been the most widely used thermal inertia map to date. Their map covers 60°N to 60°S latitude, 81% of the planet, at 2° resolution (120 km at the equator). They found values ranging from about 40 to 630 and confirmed the bimodal anticorrelation. Hayashi *et al.* (1995) reanalyzed the thermal inertia results of Palluconi and Kieffer with the inclusion of a dusty radiative–convective atmosphere. They found that thermal inertias were typically 50 J m^{-2} K^{-1} $s^{-\frac{1}{2}}$ lower than Palluconi and Kieffer had estimated. Paige *et al.* (1994) and Paige and Keegan (1994) mapped thermal inertia for the regions poleward of 58° latitude. They found similar values as did Palluconi and Kieffer where the two maps overlapped and values as high as 2000 for the north polar cap, consistent with surface water ice. Christensen and Malin (1988) reported $\frac{1}{2}$° resolution (30 km at the equator) thermal inertia within the 60°N to 60°S latitude band. They found a wider range of thermal inertia (20 to 1050). Selivanov *et al.* (1998) reported thermal-inertia maps derived from the Phobos-2 TERMOSCAN thermal images with a maximum resolution of 1.8 km. While the geographic coverage is limited, their results indicate a great deal of variability of the surface at this smaller scale. Betts *et al.* (1995) reported the thermal inertia of the south flank of Arsia Mons derived from the TERMOSCAN temperature measurements in shadow of the moon Phobos. Most recently, Jakosky *et al.* (2000) reported comparisons of a Viking-based thermal inertia map with thermal inertia maps derived from the MGS Thermal Emission Spectrometer aerobraking and science-phasing mission data at 2° resolution.

In this work we present our initial results of the derivation of thermal inertia of the martian surface at approximately 3-km resolution from mapping-mission nighttime surface-temperature observations from the MGS Thermal Emission Spectrometer. We describe our method for deriving thermal-inertia values, present global-scale mapping and analysis results, and place these results into context with previous work. We also present a selection of local high-resolution maps.

OBSERVATIONS

After the completion of aerobraking the MGS spacecraft entered the mapping phase of its mission in March of 1999, where it will map the martian surface for nominally one full Mars year. In its mapping phase the MGS spacecraft is in a nearly circular 400-km polar orbit with equator crossing at approximately 2 AM and 2 PM local Mars time. The TES is primarily nadir pointing, making surface observations every 2 s during both day and night. Each of six 8.3 mrad-IFOV detectors, arranged 2×3, provide a nominal 3×3-km resolution at the martian surface. Unfortunately, difficulties in achieving the desired mapping orbit have forced the spacecraft to orbit in a direction opposite to the original design. As a result the TES image motion compensation has been disabled and the field of view of each detector is smeared approximately 6 km downtrack. Global coverage is expected throughout the course of the mission. Three boresighted instruments include a 6- to 50-μm spectrometer, a 0.3- to 2.7-μm visible broadband channel, and a 5.5- to 100-μm thermal bolometer (see Christensen *et al.* (1992) for a full description of the TES instrument). Temperatures can be determined from the measured spectral radiance to obtain an estimate of the surface kinetic temperature and from the thermal bolometer to obtain a planetary brightness temperature. In the present work, TES orbits 1583–3814 (also called "ocks," orbits measured since Mars orbit insertion) are used, which cover the range of L_S 103° to 196°. These data were obtained from March through August of 1999.

We derive thermal inertias from both spectral and bolometric temperatures. We use a Viking-IRTM-equivalent 20-μm band temperature for a spectrometer-based thermal inertia by integrating the brightness temperature in each spectral channel weighted with the IRTM 20-μm-channel response function (Kieffer *et al.* 1977). The use of the 20-μm band provides good signal-to-noise at observed day and nighttime temperatures, with minimal interference from atmospheric dust or clouds, and it allows us to readily compare results with Viking-era thermal inertias (e.g.,

Jakosky *et al.* 2000). The bolometric temperature includes the effects of surface thermal emission, absorption by the atmosphere of emitted radiation, and thermal emission by the atmosphere. Spectral and bolometric temperatures typically differ, depending on the time of day. It is therefore important that derived thermal inertias account for all these effects.

Single observations are made of each location on the surface along a ground track. Temperature measurements at more than one time of day for single location are atypical and extremely limited in spatial coverage. For this reason we have undertaken to derive thermal inertia from single temperature measurements.

METHODOLOGY

Most previous efforts to derive thermal inertia of the martian surface commonly relied on acquiring temperature data over a finite portion of the diurnal cycle at a given location or region and then fitting a model diurnal temperature curve to this data. The fit was achieved by varying both albedo, to raise and lower the mean temperature, and thermal inertia, to match the diurnal amplitude and phase (e.g., Palluconi and Kieffer 1981, Hayashi *et al.* 1995). While this approach is suitable for data covering a diurnal cycle, it is not suitable for TES single-point temperature observations. In addition, the two parameter-fit yields a thermally derived albedo that differs significantly from the observed albedo, a result that is still poorly understood.

In the present work we develop a technique for deriving thermal inertia from single nighttime temperature measurements. As with previous efforts, our method relies on finding the thermal inertia that produces model temperatures that best fit the observations. In short, we precompute a large number of diurnal temperature cycles from a numerical thermal model for a variety of physical conditions (albedo, thermal inertia, surface pressure, dust opacity, and latitude) to generate a lookup table (totaling seven dimensions, with time of day and season). We then correlate each temperature observation with other data (e.g., latitude, albedo, time of day, etc.) and interpolate through this lookup table to find the best fitting thermal inertia. In the remainder of this section we will describe the numerical thermal model, the correlated data, the interpolation scheme, and the uncertainties associated with our method. (Our method was also used by Jakosky *et al.* (2000) in analyzing aerobraking and science phasing mission data, and is described in detail in the present work.)

The thermal model used to generate the lookup table is similar to the model that Haberle and Jakosky (1991) used to examine the effects of atmospheric radiation on the surface energy budget at the Viking Lander 1 site. In brief, subsurface temperatures are found by solving the conduction equation with the surface boundary condition,

$$\frac{S}{R^2}(1-A)\cos(i) + F_{\mathrm{IR}} + L\frac{\partial m}{\partial t} + I\sqrt{\frac{\pi}{P}}\frac{\partial T}{\partial Z'}\bigg|_{Z'=0} = \varepsilon\sigma T_{\mathrm{S}}^4. \tag{2}$$

The first term represents insolation, where S is the solar flux at 1 AU, R is the orbital radius in AU, A is the surface albedo, and i is the solar incidence angle, which varies with time of day and season. The second term represents the thermal radiation from the atmosphere, determined from an atmospheric radiative–convective model. The third term represents seasonal CO_2 condensation which occurs when the surface temperature falls below the condensation temperature of the atmosphere, where L is the latent heat of sublimation of CO_2 and m is the mass of CO_2 frost. The fourth term represents subsurface conduction, where I is the thermal inertia, P is the diurnal period, T is the temperature, and Z' is the depth below the surface normalize to the thermal skin depth. The last term represents radiation loss to space, where ε is the emissivity of the "soil" surface or CO_2 if present, σ is the Stefan–Boltzmann constant, and T_{S} is the surface temperature. With the depth normalized to the thermal skin depth, it becomes clear that the thermal inertia is the key parameter relating subsurface conduction and heat storage to the surface temperature. The thermal skin depth, δ, can be expressed as

$$\delta = \frac{I}{\rho c}\sqrt{\frac{P}{\pi}}. \tag{3}$$

The primary differences between the model of Haberle and Jakosky (1991) and the present model are in its extension to include seasonal cycles and correcting the physics to incorporate the wide range of conditions found in TES observations.

Components of the atmospheric model are described in detail by Pollack *et al.* (1990) and references therein. This model incorporates solar and thermal infrared radiative transfer in a dusty, CO_2 atmosphere. It determines attenuation of solar radiation incident on the surface, emission of thermal radiation by the atmosphere (downward onto the surface and upward from the top of the atmosphere), and attenuation of thermal radiation emitted by the surface before reaching space. This atmospheric model also includes the potential effects of condensation of CO_2 within the atmosphere, convective instability, and sensible heat exchange with the surface.

The surface and subsurface temperatures are calculated by a standard thermal model, where the thermal diffusion equation is solved for subsurface temperatures by a forward-time finite-difference method, with the appropriate boundary conditions. The lower boundary is below the depth of penetration of the seasonal thermal wave and is assumed nonconducting. The upper boundary is the surface temperature, which is found by an instantaneous solution of Eq. (2). Some of the basic physical parameters we adopted as constant in the present work are listed in Table I.

The calculations proceed by iterating the surface and subsurface temperatures 144 times each martian day and the atmospheric temperatures every 24th of a martian day. Model calculations repeat for 3 Mars years to eliminate initial conditions. The lookup table is generated by computing diurnal and seasonal temperatures for each combination of interpolation parameters

TABLE I
Additional Model Parameters

Material	Property	Value	Units
CO_2	Frost temperature[a]	T_F	K
CO_2	Sublimation latent heat	5.9×10^5	J kg^{-1}
CO_2 frost	Infrared emissivity	0.8	
CO_2 frost	Albedo	0.65	
Regolith	Infrared emissivity	1.0	
Regolith	Specific heat capacity[b]	627.9	J kg^{-1} K^{-1}
Regolith	Bulk density[b]	1500	kg m^{-3}

[a] The surface temperature at which CO_2 frost forms is given by $T_F = 149.16 + 6.476 \ln(0.13499P)$, where P is the surface pressure in mb.

[b] Surface temperature is independent of the choice of heat capacity and density; only the depth distribution of subsurface temperatures depend on these parameters (see Eq. (2)); values are given here for reference.

(thermal inertia, albedo, dust opacity, and surface pressure) at every 5° of latitude. Model temperatures (a surface kinetic temperature and a bolometric blackbody temperature) are saved for each 24th of a martian day at 8-day intervals throughout the martian year. These parameters and intervals make a total of seven dimensions for later interpolation.

Figure 1 shows examples of the dependence of the diurnal temperature on thermal inertia, albedo, dust opacity, and surface pressure for the specific interpolation nodes used. Thermal inertia has the largest influence on the surface temperature. Ten values were chosen from 24 to 800, logarithmically spaced. High values of thermal inertia generally cause surface temperatures to remain cool during the day and warmer at night and shift the peak temperature to later in the afternoon. TES observations are primarily restricted to 2 AM and 2 PM local time, except for near the poles. Temperatures near dusk or dawn are not uniquely related to thermal inertia, so these times of day are not preferred. Albedo and pressure have the effect of raising or lowering the average temperature. Increasing dust opacity affects the surface temperature in a manner similar to thermal inertia, cooling the surface during the day and warming the surface at night; therefore, a higher-than-anticipated dust opacity can result in deriving a higher thermal inertia than represents the true surface.

For each TES temperature measurement, correlated values are needed for each axis in the lookup table, except thermal inertia. Latitude (and longitude), time of day, and season are readily determined from the spacecraft ephemeris. In addition, albedo, surface pressure, and dust opacity are needed. Albedo is retrieved from a $\frac{1}{4}^\circ$ map derived from TES daytime albedo observations

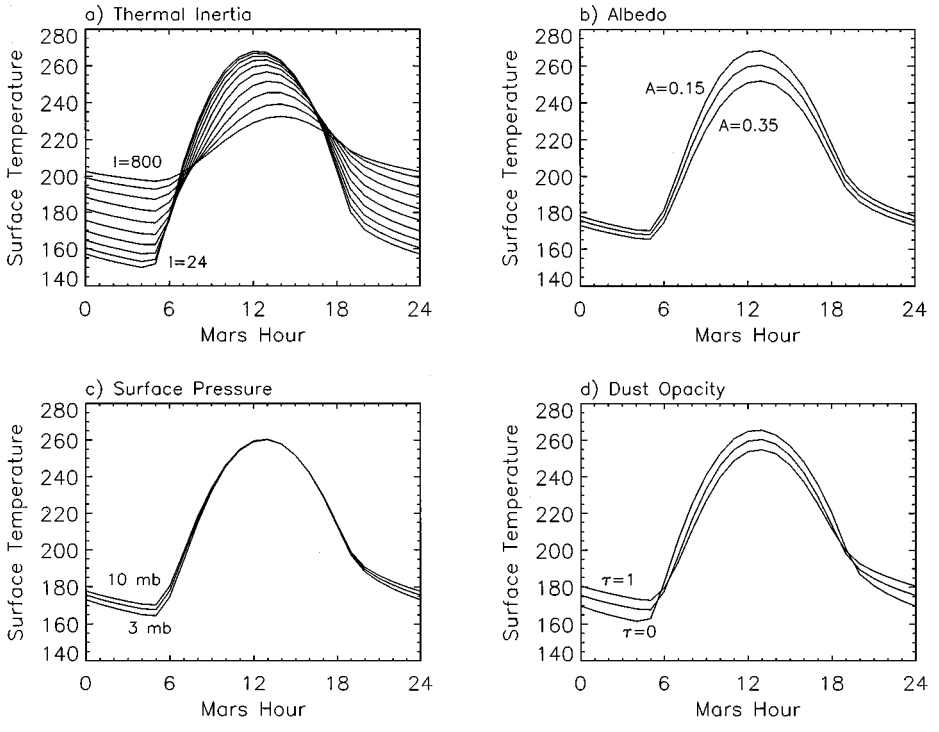

FIG. 1. Examples of diurnal variations in surface temperature for different values of independent physical properties used as interpolation nodes in deriving thermal inertia. (a) Thermal inertia. Thermal inertias nodes are 24, 35.43, 52.32, 77.24, 114, 168.4, 248.6, 367, 541.9, and 800 in units of J m^{-2} K^{-1} s$^{-\frac{1}{2}}$. The largest amplitude diurnal temperature cycle corresponds to the lowest thermal inertia and the lowest amplitude cycle corresponds to the highest thermal inertia. (b) Albedo. Albedo nodes are 0.15, 0.25, and 0.35. Lower albedos raise the surface temperatures at all times of day. (c) Pressure. Atmospheric surface pressure nodes are 3, 6, and 10 mb. The lower pressures results in the lower nighttime surface temperatures. Daytime temperatures are minimally effected. (d) Dust opacity. Atmospheric infrared dust opacity nodes are 0, 0.5, and 1.0. Higher dust opacities have the same effect as higher thermal inertias, to reduce the amplitude of the diurnal cycle. All temperatures are given for 50° latitude and an L_S of 38.8°. Invariant parameters in each figure are 114 for fixed thermal inertia, 0.25 for fixed albedo, 6 mb for fixed pressure, and 0.5 for fixed dust opacity.

(Christensen 1999); at this resolution the map contains about 65% coverage in the region 62°S to 87°N, with missing values filled by interpolation. For the polar regions, not mapped in the present work, Viking IRTM albedos are used (Paige *et al.* 1994, Paige and Keegan 1994). Surface pressure is estimated from a combination of a MGS Mars Orbiter Laser Altimeter (MOLA) 1° map of elevation (Smith *et al.* 1999) and a seasonal pressure model developed by Tillman *et al.* (1993) from Viking Lander 1 surface pressure observations for the Viking Lander 1 elevation from MOLA data of −3.72 km. To extrapolate surface pressure to other elevations we assume a scale height of 10.8 km. We assume a dust opacity of 0.1 at thermal IR wavelengths normalized to 6.1 mb, consistent with TES spectral observations for the orbits presented here (M. D. Smith, pers. commun. 1999). It is expected that dust opacity will be spatially and temporally variable; these values are not presently available and so we do not account for this effect in the present work. We do include the effects of topography on the column opacity, scaled with surface pressure. For dust opacity at visible wavelengths we multiply the IR dust opacity by 2 (Haberle and Jakosky 1991).

For every observed temperature, quadratic interpolation is performed on each lookup-table axis of albedo, pressure, and dust opacity. For hour and latitude we employ a bicubic spline interpolation. Season is interpolated linearly. Last, the observed temperature is interpolated linearly in log of thermal inertia to obtain the derived value. Interpolation functions and node spacing were chosen to minimize interpolation errors, while keeping computing needs tractable.

Uncertainty in the derived thermal inertia is introduced at three primary stages: in the measured temperature, in the thermal model that is used to generate the lookup table, and in the interpolation scheme. For a model-dependent derivation of this level of complexity, uncertainty can only be estimated. Estimates of these uncertainties are summarized in Table II for a nighttime surface temperature of 180 K based on instrument and model performance. Christensen *et al.* (1992) report expected instrument noise levels for the bolometer and spectrometer. In practice, spectrometer noise levels are slightly higher than anticipated due to spacecraft electronic interference. The spectrometer temperature-measurement uncertainty listed in Table II includes this increased noise level. Thermal model performance is tested by comparing results with analytic solutions of special endmember cases and to asymptotic behavior. Interpolation error is evaluated by comparing direct thermal calculations to interpolated approximations. The total uncertainty in Table II should be considered an upper limit estimate, since we have assumed that all errors are positive and systematic and therefore add.

In practice, thermal inertia varies smoothly over horizontal downtrack distances and good agreement is observed between spectrometer-based and bolometer-based values, both suggesting that actual errors are less than reported here. A fourth source of uncertainty is introduced in the other input values that are correlated with temperature and in thermal model physics that has not been included. For example, dust opacity is assumed to be spatially and temporally invariant, which is certainly not the case; temporal changes in dust opacity manifest in discontinuous changes in thermal inertia between adjacent ground tracks (discussed below). Regional surface slopes that affect the local solar incidence angle are also not included. In addition, spatial variations in surface thermal emissivity are not accounted for in temperature calculations. Nonunit emissivity does not significantly affect the bolometer-based thermal inertia, which compares model and observed brightness temperatures both assuming unit emissivity. Spatial variability in spectral emissivity does introduce variability in the spectrometer-based thermal inertia that is related to mineralogical units (see discussion below).

RESULTS AND DISCUSSION

In this section we will present results of thermal inertia derivation from TES observations. First we will present global-scale results and analysis of potential correlation with other properties. We will then focus on some selected regions for high-resolution mapping. Throughout this section we will compare our results with previous studies, confirming some previous conclusions and presenting some new interpretations.

Global Mapping of Thermal Inertia

Figure 2 shows a global map of thermal inertia derived from the TES bolometer observations of the brightness temperature of Mars, mapped at a resolution of 4 pixels per degree (about 15 km at the equator). Since global coverage has not yet been achieved, this map has been filled by interpolation for the regions between 50°S and 70°N latitude. Figure 3 shows a map of the coverage of thermal inertia prior to filling; at this resolution approximately 63% of the surface in this latitude range contains TES-derived thermal inertias. Gaps occur along ground tracks

TABLE II
Uncertainty Estimates for Each Step in Thermal Inertia Computation

	TES measurement	Thermal model	Interpolation							Total uncertainty
			Inertia	Albedo	Pressure	Opacity	Hour	Season	Latitude	
Bolometer	2.7	1.4	0.10	0.10	0.65	0.10	0.50	0.25	0.20	6.0
Spectrometer	13.6	1.8	0.10	0.10	0.20	0.10	0.50	0.25	0.20	16.9

Note. Uncertainties are for a 180 K surface temperature, nighttime observation. All values are given in percentage of the derived thermal inertia.

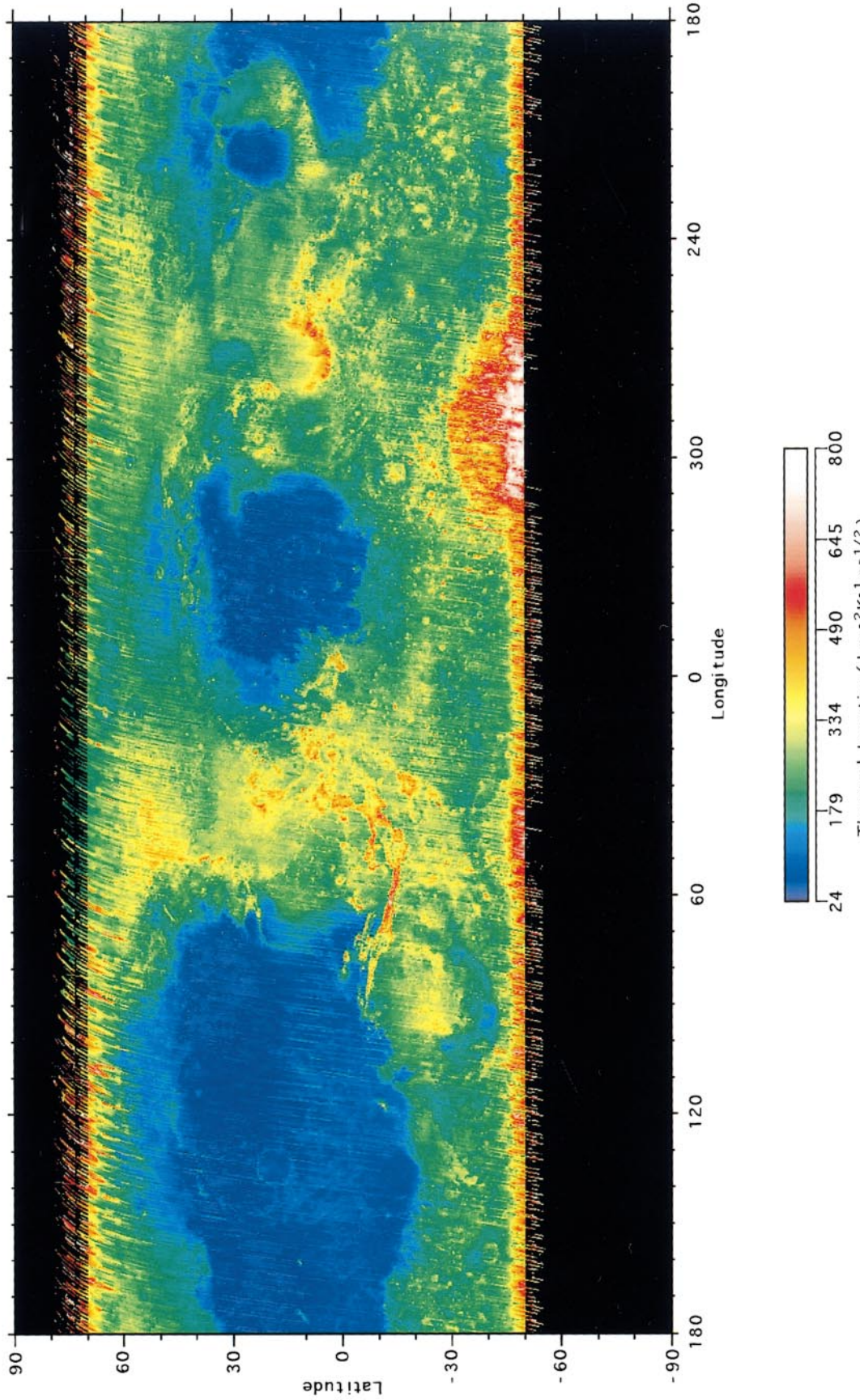

FIG. 2. Nighttime bolometric thermal inertia map. Thermal inertias are mapped at a resolution of $\frac{1}{4}^{\circ}$ per pixel from TES orbits 1583–3814. Interpolation is used to fill missing data between TES ground tracks for latitudes 50°S to 70°N. Besides the global pattern of low and higher thermal inertia, significant small-scale structure can be seen. See text for discussion.

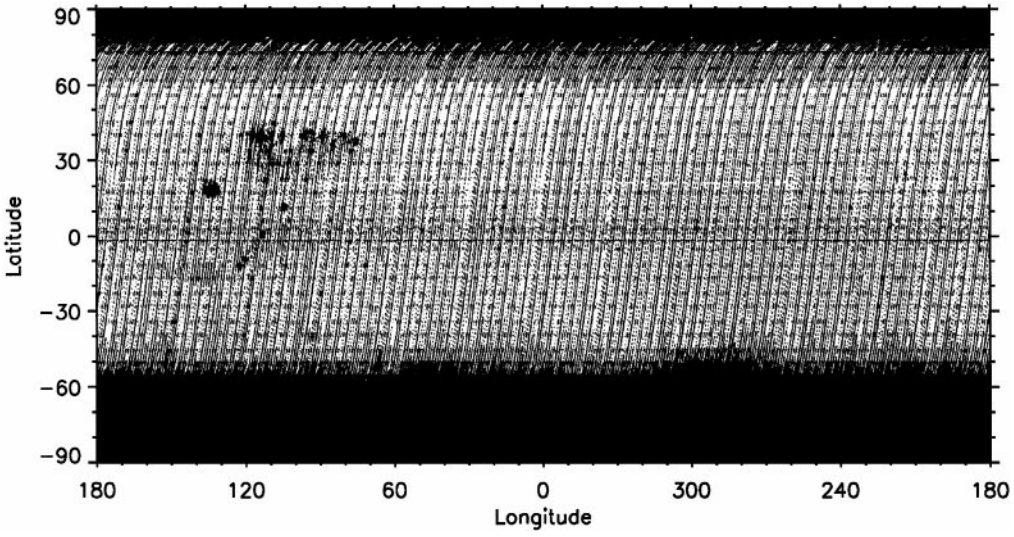

FIG. 3. Coverage of data in Fig. 2, prior to filling by interpolation. Approximately 63% of the map contains TES-derived thermal inertia in the latitude range 50°S to 70°N. Gaps along ground tracks result from limb and calibration observations. Some missing coverage in the Tharsis region (70° to 140°W) is due to surface temperatures consistent with thermal inertias less than 24, which fall outside the derived range. Smaller areas with surface temperatures consistent with thermal inertias over 800 are also not plotted but are present.

due to calibration and limb observations. Other gaps occur when temperatures fall outside the range in the lookup table, indicating thermal inertias higher than 800 or lower than 24. The map in Fig. 2 incorporates data from TES orbits 1583 (the beginning of mapping) to 3814. This range covers L_S 103° to 196°. On a global scale we see the same regional pattern of high and low thermal inertia as was seen in Viking IRTM-based thermal inertia (see Jakosky *et al.* (2000) for a discussion). In addition, a great deal of fine structure can be seen that commonly, but not always, correlates with visible smaller-scale geologic features. High-resolution data will be discussed in the next section.

Several features seen in the global map are artifacts of processing for these seasons. Roughly north–south trending streaks are prevalent near the northern boundary of the map and fainter streaks are present throughout the map. These streaks are a result of our assumption of a constant dust opacity. While the infrared dust opacity of 0.1 used in processing these orbits is representative of this time period, small temporal variations cause streaks in spatially adjacent ground tracks taken a month or more apart. In addition, at the north and south edges of the mapped area the apparent thermal inertia increases. In the north, this may be due to the proximity of the observations to the polar terminator and possibly complicated by the presence of clouds. Both are conditions where our algorithm does not do well and results in an overestimate of the thermal inertia. The south boundary of the thermal inertia map nears the edge of the seasonal CO_2 polar cap, where surface temperatures are at or near the CO_2 frost temperature. When observations fall within 5° in latitude of this boundary (one lookup-table latitude step) the error associated with the latitude interpolation increases greatly. The high thermal inertia region located at about 30°S to 50°S and 270°W to 310°W is associated with the Hellas impact basin. The likelihood of relatively high column dust opacity and CO_2 surface frost makes these values suspect. As the seasonal polar cap recedes, these areas should be revealed with greater confidence.

Comparison between thermal inertia derived from the bolometer observations of brightness temperature and from spectrometer 20-μm temperature is shown in the 2D histogram in Fig. 4. (Histograms utilize maps prior to filling by interpolation.) Aside from infrequent outlying points, the correlation between bolometer-based and spectrometer-based thermal inertia is quite good. At the lowest thermal inertia the two agree within the level of uncertainty discussed above. At higher thermal inertia the spectrometer-based values are consistently about 5–15% lower; for example, at a bolometer-based thermal inertia of 250 the spectrometer-based thermal inertia is on average about 25 lower. Although still within the estimated upper-limit uncertainty, we think this difference is significant and represents a difference in the surface emissivity of the 20-μm band between high and low inertia regions. Christensen (1982), in examining IRTM data, found that the 20-μm emissivity varied with albedo from about 0.98 for bright regions to 0.92 for dark regions. For a bright, low-thermal-inertia region, an emissivity of 0.98 would reduce the nighttime spectral brightness temperature by less than 1 K and result in a derived thermal inertia only 2 less than for unit emissivity (see Fig. 1a). However, for dark high-thermal-inertia regions, an emissivity of 0.92 would reduce nighttime spectral brightness temperature about 6 K and the derived thermal inertia by about 25, relative to a unit-emissivity surface. These effects are consistent with the magnitude and sign of the difference between the spectrometer and bolometer-based thermal inertias. In general, since bolometer-based thermal inertias are not significantly affected by nonunit emissivity, these values are more representative of the physical character of the surface.

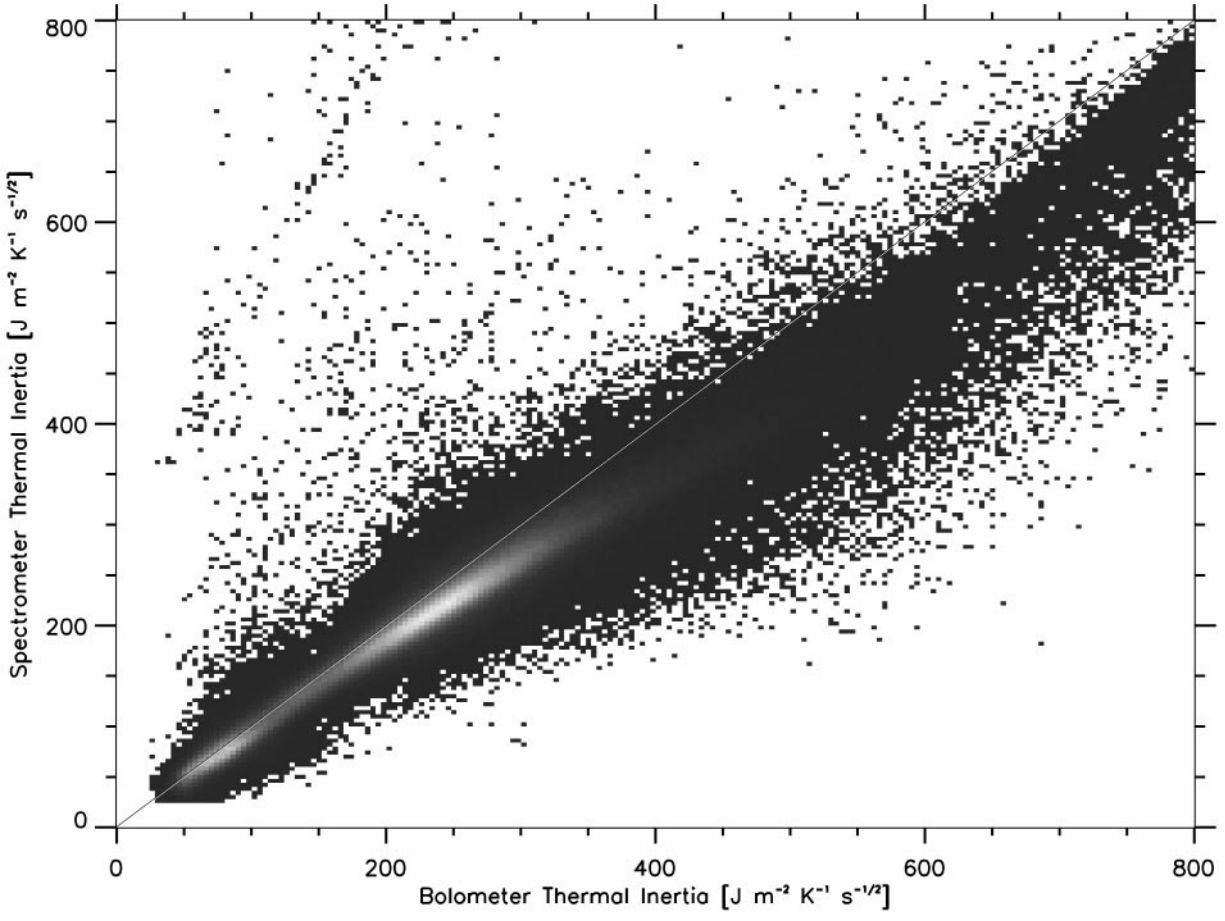

FIG. 4. Two-dimensional histogram of spectral and bolometric nighttime thermal inertia. Histogram density is shown in shades of gray. White represents no occurrence. The darkest gray indicates a frequency of 1 map location per bin. The lightest gray is a maximum frequency of 1373. Points falling on the $x = y$ line indicate perfect agreement between the two sets of data. A strong agreement is observed. The bin size is 4 J m^{-2} K^{-1} s$^{-\frac{1}{2}}$. See text for a discussion.

From the overall regional agreement with the Viking-based thermal inertia maps (Jakosky *et al.* 2000) and the good correlation between bolometer and spectrometer thermal inertias, these results indicate that the our method for deriving thermal inertia works well. We believe that, in addition to the significantly higher resolution, our method represents an improvement over earlier calculations. Furthermore, the consistency between spectrometer and bolometer thermal inertias provides confidence that uncertainties are less than the values reported in Table II.

In Fig. 2 three large areas of low thermal inertia appear in Tharsis, Arabia, and Elysium. Thermal inertia values in these region are typically lower than about 150 and are contained within a distinct boundary. Previous interpretations of these three low thermal inertia regions suggest that they are composed of deposits of loose fine-grained material (dust perhaps with a mean diameter of less than 40 μm) to a depth of more than several diurnal skin depths (e.g., Kieffer *et al.* 1977, Zimbelman and Kieffer 1979, Palluconi and Kieffer 1981, Christensen 1982). For the heat capacity given in Table I, a density of 1200 kg m^{-3}, and a thermal inertia of 75, one diurnal skin depth is about 1.6 cm. For a higher thermal inertia of 250 and a corresponding density of 1600 kg/m^3, the diurnal skin depth is about 4 cm. Few rocks or coarse surface materials are exposed in these low-thermal-inertia regions (Christensen 1986, Jakosky and Christensen 1986a). Radar data also suggests a relatively thick, low-density material which supports this conclusion (Jakosky and Christensen 1986a).

The higher thermal-inertia regions are more complex. They have been interpreted as possibly containing more surface rocks or exposures of bedrock, larger particle sizes, and/or indurated fines forming a duricrust (e.g., Kieffer *et al.* 1977, Palluconi and Kieffer 1981, Christensen 1986, Jakosky and Christensen 1986a, Christensen and Moore 1992). Christensen (1986) mapped the abundance of surface blocks (rocks and bedrock) from Viking IRTM data and separated the rock component from the fine component thermal inertia. His results indicated that the coverage of blocks was typically 6% with a few surfaces as high as 25%. While there is a correlation between thermal inertia and rock abundance, it was found that the fine component dominated the total thermal inertia of the field of view. Therefore, while

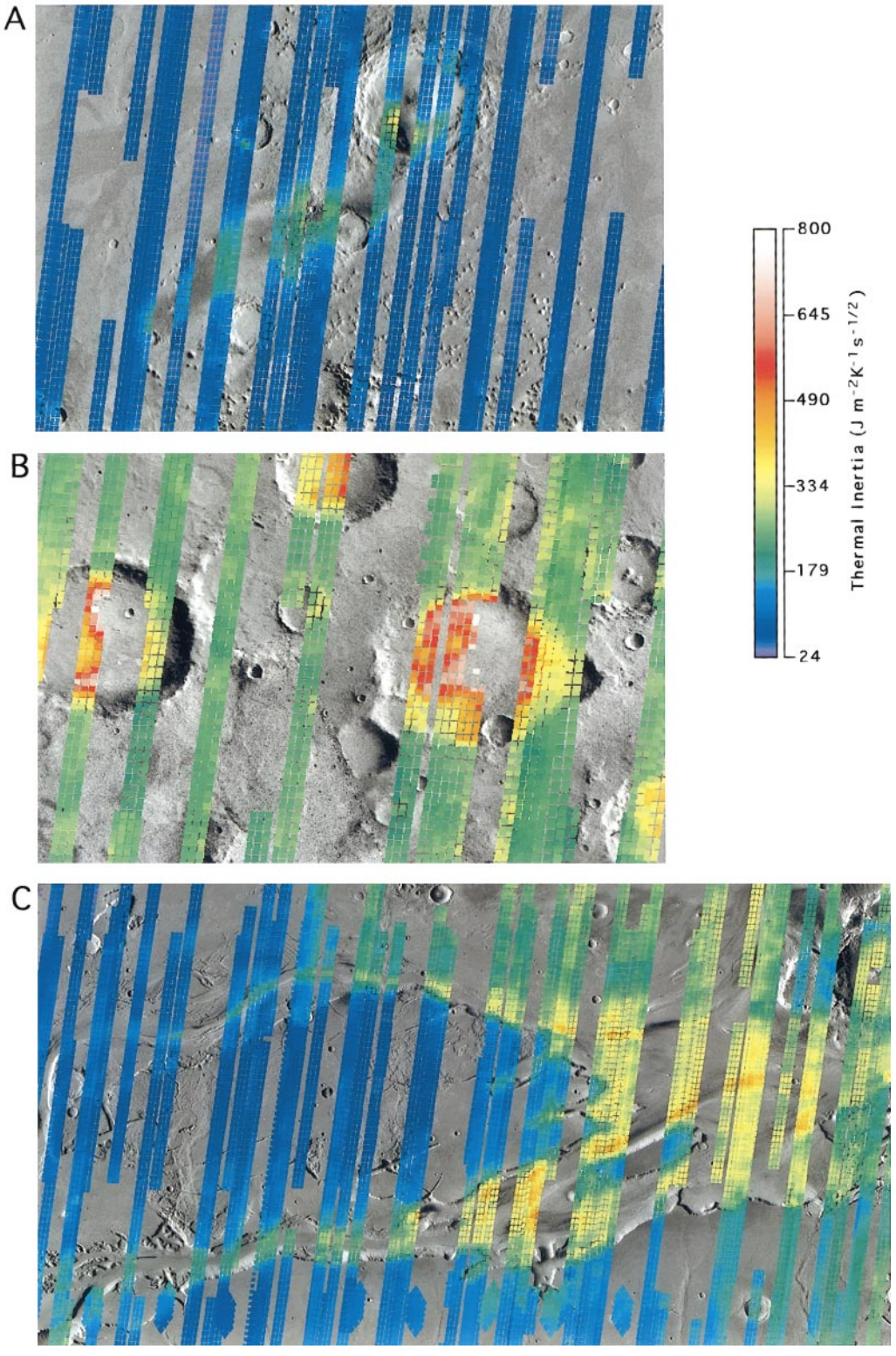

FIG. 9. High-resolution maps of nighttime bolometric thermal inertia. Color pixels represent TES 3-km foot prints. North–south trending stripes represent MGS orbit ground tracks. Adjacent ground tracks are obtained 1 month or more apart. Underlying basemap images are USGS Viking mosaics. To account for the present differences in the USGS cartographic reference frame and the MGS inertial frame, basemap images are linearly transposed to align topographic and albedo features with thermal inertia features. Confidence in the realignment is obtained by correlating several features at different locations. Linear shifts are typically less than about 30 km. Uncertainty in the correlation is less than about 2 TES pixels (6 km). For scale, TES pixel size is about 3 km. North is up in all maps. Maps shown are: (A) Pettit crater and wind streak, 12°N × 174°W; (B) high inertia craters in the southern highlands, 28°S × 334°W; (C) Kasei Vallis, 25°N × 66°W; (D) Ophir Chasma, 4°S × 72°W; (E) Coprates Chasma, 14°S × 59°W; (F) high/low thermal inertia boundary near Elysium, 27°N × 193°W; and (G) thermal inertia boundary near Daedalia Planum, 35°S × 137°W.

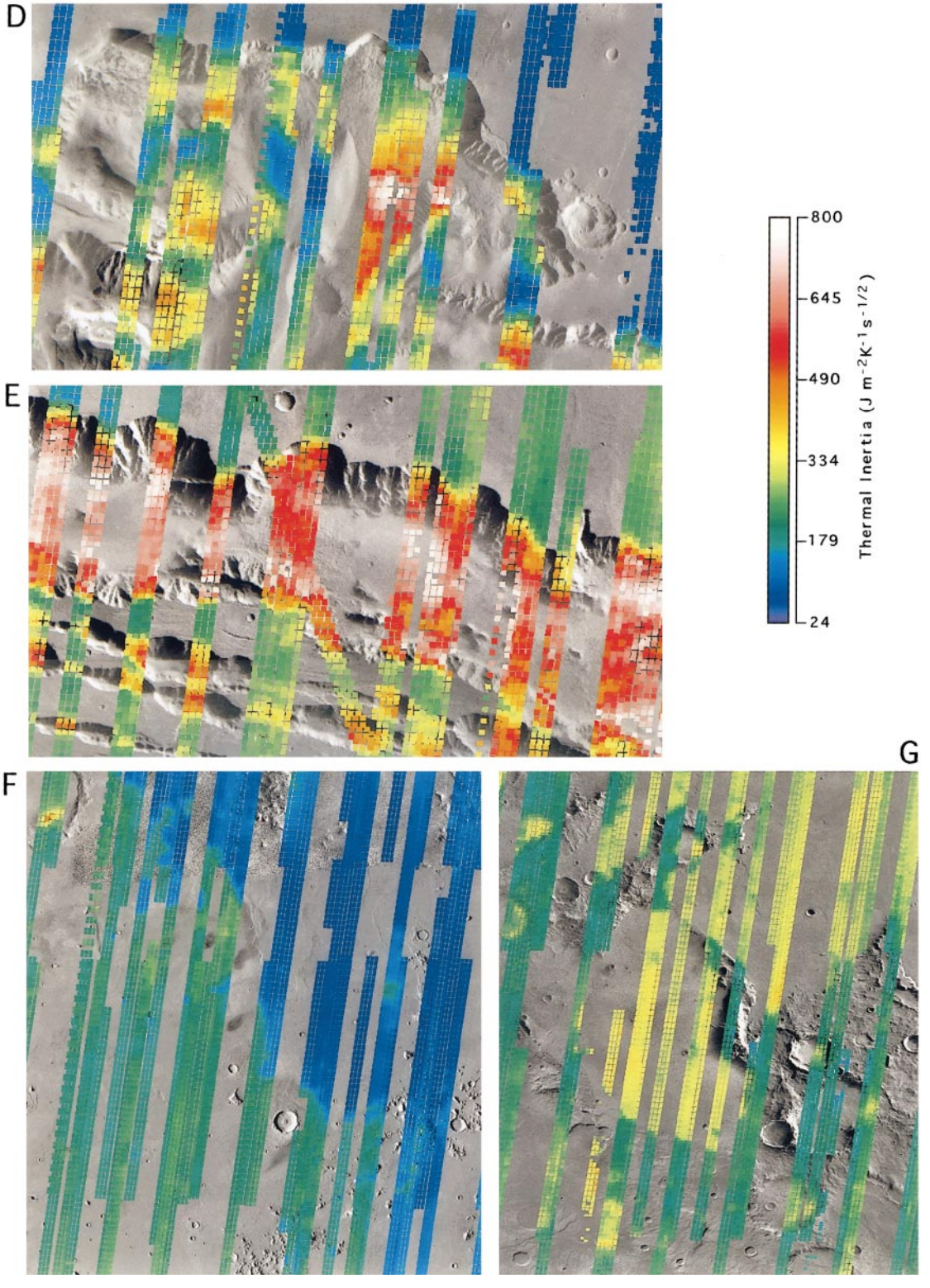

FIG. 9—*Continued*

abundant rocks and bedrock do have the effect of slightly raising the thermal inertia in the field of view, it is the effects of the fine material at the surface that is primarily distinguished from orbit. This result may depend in part on the overall low rock abundances. As higher resolution is achieved, a wider range of thermal inertia is discerned and true exposures of bedrock may be located.

Thermal inertia has also been related to particle size (e.g., Kieffer *et al.* 1973, Palluconi and Kieffer 1981, Jakosky 1986). Assuming a uniform particle size and a smooth, homogeneous surface, the thermal conductivity of the bulk material is strongly affected by the particle diameter (e.g., Wechsler and Glaser 1965, Presley and Christensen 1997), varying by several orders of magnitude, while density and heat capacity change little. Therefore, thermal inertia will also vary significantly with particle size (see Eq. (1)). Some geological processes may act to generate grains of specific sizes (chemical and physical weathering) and to sort grains into size ranges (aeolian and fluvial redistribution). In these geologic contexts interpreting thermal inertia in terms of a mean particle size would be quite informative. However, Kieffer (1976) pointed out that the thermal inertia of the Viking landing sites, derived from the IRTM and adjusted for the observed rock abundances, could not be reconciled with the observed particle size; the derived thermal inertia indicated much larger particles than were observed, leading to the hypothesis that the bonding of soil grains by salts (forming the observed "duricrust") might account for the higher thermal inertia.

Cementing of soil grains can affect the thermal inertia by increasing the efficiency of heat conduction between individual grains by forming or enlarging the contact area. Induration of the surface layer has been observed at the Viking and Pathfinder landing sites (Mutch *et al.* 1977, Binder *et al.* 1977, Moore *et al.* 1999) and may be widespread (e.g., Ditteon 1982, Jakosky and Christensen 1986a,b, Christensen and Moore 1992). Salt has been suggested as a cementing agent due to the high concentrations of sulfur and chlorine in the soil at these same locations (Clark *et al.* 1982, Moore *et al.* 1999). It has also been suggested that the degree of induration could account for much of the variations in thermal inertia observed outside the lowest thermal inertia regions (Jakosky and Christensen 1986a,b, Christensen and Moore 1992).

A great deal can be learned about the nature of the martian surface from correlations between thermal inertia and other data sets. An interesting correlation has previously been observed in Viking data when comparing thermal inertia with albedo (e.g., Palluconi and Kieffer 1981). Cross comparison had revealed a strong bimodal anticorrelation (shown in Fig. 5a as a 2D histogram). The low-thermal-inertia regions were limited to high albedo with a modal peak thermal inertia of 105 and an albedo of 0.30. The high-thermal-inertia regions were almost always low albedo with a broad modal peak thermal inertia of about 270 and an albedo of around 0.20–0.23 (see Table III). A similar analysis using TES data is shown in Fig. 5b as a 2D histogram of TES albedo versus bolometer-based thermal inertia. This histogram

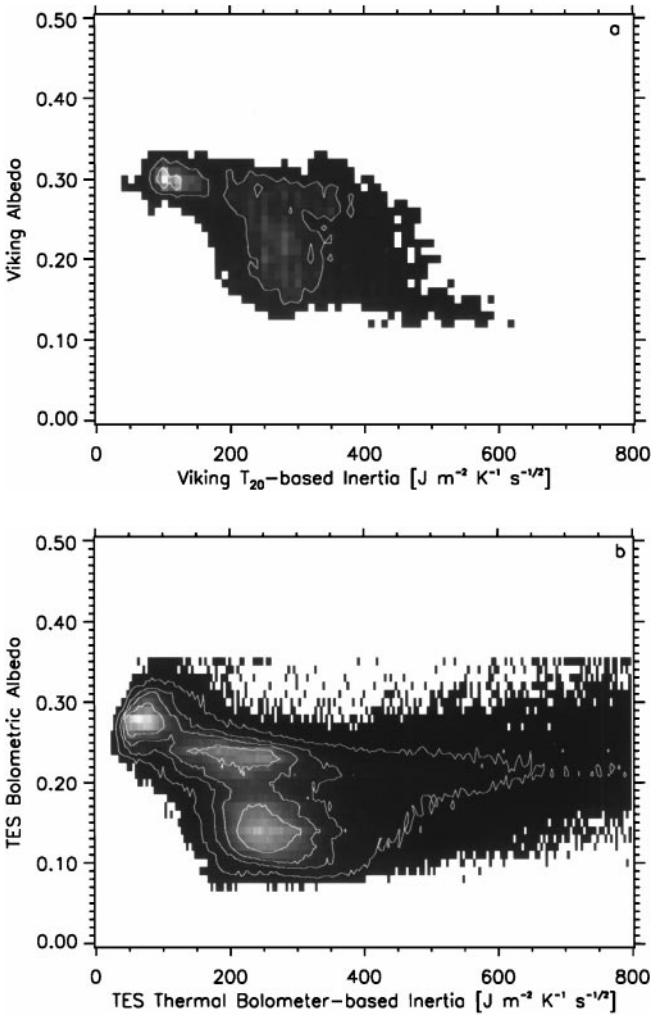

FIG. 5. Two-dimensional histogram of (a) Viking IRTM albedo and 20-μm thermal inertias (Palluconi and Kieffer 1981) and (b) MGS TES bolometric albedo and nighttime bolometric thermal inertia. White represents no occurrences. The darkest gray indicates a frequency of 1. In the Viking histogram (a), two modes of frequent correlation occur, while in the TES histogram (b), three separate modes of frequent correlation are evident. The low-thermal-inertia/high-albedo and high-thermal-inertia/low-albedo modes are observed in both cases. A new moderate-to-high thermal inertia and intermediate albedo mode is found in the current TES analysis. Contours intervals are frequencies of 20, 100, 200, and 400 per bin. Albedo bin size is 0.01. Thermal inertia bin size is 4 for TES and 10 for IRTM.

shows a clear trimodal behavior. The two previously observed modes are evident, low-thermal-inertia/high-albedo and high-thermal-inertia/low-albedo with a slight shift to in their peaks (see Table III, TES modes A and B). The new, third, mode has a moderate-to-high thermal inertia and an intermediate albedo. The peak of the new mode has a thermal inertia of 180–250 and a narrow range of albedo near 0.24.

Figure 6 shows individual histograms of TES bolometer-based thermal inertia and TES albedo in comparison with Viking IRTM thermal inertia and albedo (Palluconi and Kieffer 1981). The TES thermal inertia histogram is bimodal with a low

TABLE III
Albedo-Thermal Inertia 2D Histogram Modes

	Mode	Inertia	Albedo
Viking	1	105	0.30
	2	270	0.20–0.23
TES	A	70–80	0.28
	B	240–260	0.14
	C	180–250	0.24

Note. Viking modes are from Palluconi and Kieffer (1981). TES modes are from this work.

TABLE IV
Mapped Thermal Inertia-Albedo Units

Unit	Inertia	Albedo
A	0–120	0.25–0.32
B	120–350	0.09–0.19
C	120–320	0.19–0.27

thermal-inertia mode of 70–80 and a high thermal-inertia mode of around 240–250. The Viking thermal-inertia histogram is similar, but shifted to higher values. The differences can be partly explained in two ways: (1) an overall shift of about 50 to lower TES thermal inertias due to the inclusion of a radiative–convective atmosphere (Hayashi *et al.* 1995, Jakosky *et al.* 2000) and (2) less of a shift for dark, high-thermal-inertia regions due to the effects of a nonunit emissivity, which were not accounted for in the Viking 20-μm thermal inertias and do not significantly affect the bolometer-based thermal inertia (see Fig. 4 and the related discussion above). Other smaller differences are due to higher TES resolution separating Viking subpixel inhomogeneities. The albedo histograms in Fig. 6, on the other hand, are dramatically different. Many regions have lower albedos in the TES observations (Christensen 1999), than in the IRTM observations (Pleskot and Miner 1981), primarily the result of clearer atmospheric conditions (low dust opacity) for the TES observations. As a result of these clear conditions we are now able to resolve regional albedo differences with greater precision and accuracy. The presence of the trimodal behavior in Fig. 5b is due to the combined effects of higher resolution and improved values of both thermal inertia and albedo. In addition, the presence of the broad high-thermal-inertia mode in the Viking-based histogram (Fig. 5a) supports the conclusion that the observation of the third mode (Fig. 5b) does not represent a change in the martian surface, but is now discerned as a result of improved observations.

We define the three modes in Table III as three thermophysical surface units: (A) low thermal inertia and high albedo, (B) high thermal inertia and low albedo, and (C) the new mode of moderate-to-high thermal inertia and intermediate albedo. The definitions of these units are described in Table IV. We map these

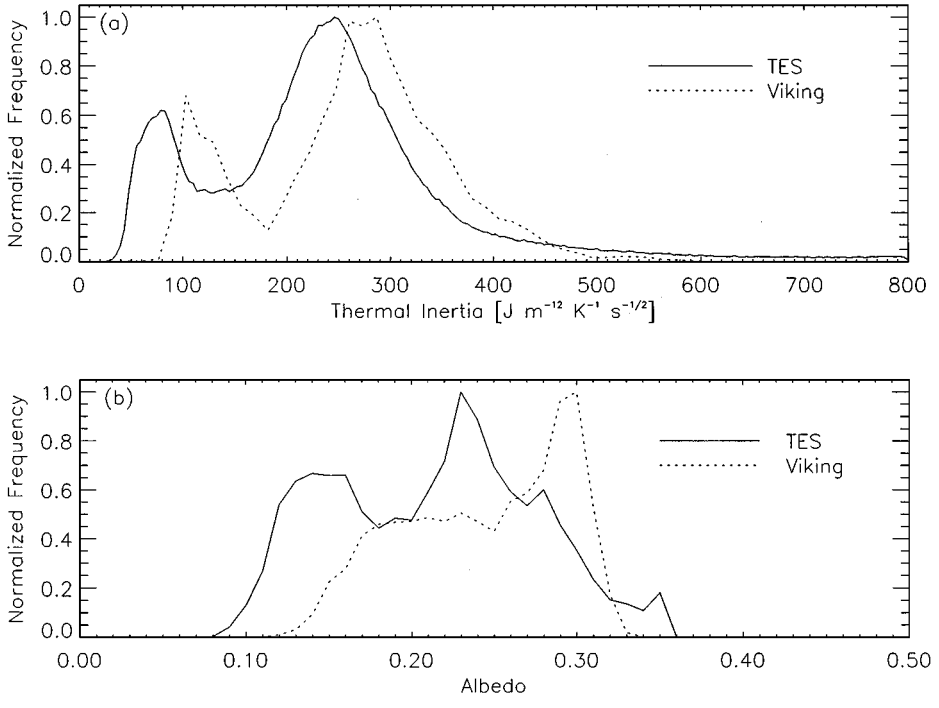

FIG. 6. Histograms comparing (a) TES bolometric thermal inertia and Viking IRTM thermal inertia from Palluconi and Kieffer (1981), and (b) TES bolometric albedo and IRTM albedo. The thermal inertia histograms look quite similar (differences are explained in the text). The albedo histograms differ primarily as a result clearer atmospheric conditions during TES observations.

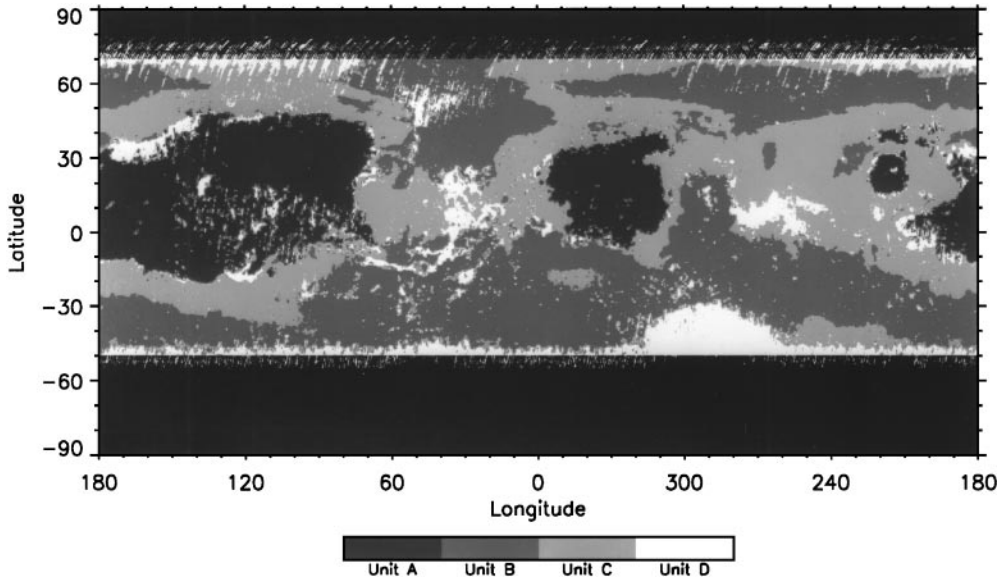

FIG. 7. Map of units in Table IV. Units represent the different thermal inertia/albedo modes in Fig. 5.

units in Fig. 7, using unit D as all locations that do not fall into the three categories. The spatial distribution of the new mode (unit C) is remarkable in that it serves as a boundary between units A and B.

It is unlikely that unit C is a gradual transition between units A and B, but instead is a distinctly different type of martian surface. From the 2D histogram in Fig. 5b, we can see the mode peak representing unit C forms a distinct cluster separate from the other modes. If unit C represented simply a gradual thinning of a thick unconsolidated dust layer in unit A exposing an underlying surface of unit B, we would expect the histogram to exhibit a smooth transition between the modal peaks of A and B. The peak representing unit C would require that the thinning plateau at some intermediate stage for a large region of the martian surface. It is important to note that albedo is sensitive to the top few tens of micrometers of the surface, while thermal inertia senses the top few centimeters. The addition of bright dust atop an initially darker, high-thermal-inertia surface would quickly brighten the surface without having any discernible effect on the thermal inertia (see also the discussion of Cerberus region below). The narrow range of relatively low albedo exhibited by unit C suggests that a dust cover would need to be optically thin over a vast lateral expanse and then rapidly thicken into unit A or vanish into unit B. This is certainly possible, though it is difficult to imagine a mechanism for maintaining a large and constantly optically thin deposit.

Another possibility is that unit C represents a thicker deposit of dust that has been cemented, raising the thermal inertia and possibly darkened by the cementing process. Presley and Arvidson (1988) proposed just such a mechanism to describe the Oxia region of Mars (centered about 10°N × 355°W) just north of Sinus Meridiani and west of Arabia. In this region they noted that the surface has a dark red color distinctly different from the more characteristic bright red and dark gray regions. They noted that the IRTM thermal inertias of this region are consistent with a particle size easily mobilized by winds, but no eolian landforms are observed in Viking images. Their conclusion was that the surface was resistant to erosion due to cementing of smaller low-thermal-inertia particles, thus raising the thermal inertia. The boundaries of this proposed indurated unit correspond extremely well with our unit C, with Arabia (unit A) to the east and Sinus Meridiani (unit B) to the south (see Fig. 7). Similar arguments for indurated soil deposits were put forth by Arvidson *et al.* (1989) for Lunae Planum, Xanthe Terra, and Oxia Palus (from about 0°–20°N × 0°–70°W) and by Merényi *et al.* (1996) for Deucalionis Regio (centered about 15°S and 350°W). Again these regions are largely dominated by our unit C, though their proposed boundaries are not as well defined. Furthermore, Christensen and Moore (1992), in examining thermal, radar, and color observations, also suggested an indurated surface unit. In the southern hemisphere, our unit C maps onto their indurated "unit 3," though significant overlap occurs onto other units. These studies, therefore, support the hypothesis that our unit C indicates the global distribution of duricrust or indurated soil material on Mars.

Interestingly, the Viking landing sites both map onto our unit C, while the Pathfinder landing site maps onto unit D. Although TES spatial coverage does not yet allow for mapping thermal inertia at these exact locations, thermal inertias derived for the general region of these landing sites are 380, 320, and 230 (±50) for Pathfinder, Viking 1, and Viking 2, respectively. These values are consistent with values derived from IRTM (Kieffer 1976, Golombek *et al.* 1999), except for Viking Lander 2, where TES values for this region are about 35% lower. Not all of this difference can be accounted for in the uncertainty, and it is unclear why TES values are lower; increased spatial coverage may help

resolve this difference. It is evident that the Pathfinder site maps onto unit D because it has a higher thermal inertia than we have chosen for unit C. Since surface and subsurface duricrusts have been observed at these landing sites, the correlation of the Viking landing sites with unit C further supports the hypothesis of this unit representing an indurated near surface layer (Jakosky and Christensen 1986a, Christensen and Moore 1992), distinctly different from units A and B.

Previous comparisons between IRTM thermal inertia and Viking-era surface elevation indicate a weak correlation on a global scale, where thermal inertia tends to decrease with increasing elevation (Jakosky 1979, Palluconi and Kieffer 1981). On a local scale Zimbelman and Leshin (1987) found no consistent correlation for the Elysium and Aeolis quadrangles. In Fig. 8A we show the TES bolometric thermal inertia histograms for each 2-km step in MOLA elevation. At the lowest elevation the thermal inertia is dominated by the Hellas impact basin; these thermal inertias are highly uncertain as discussed above. In the −6- to −4-km bin only the higher thermal inertias are present. From −4 to 6 km both low and high thermal inertia surfaces are present. Within this elevation range there is some evidence that the two peaks in the histogram are converging, with the low thermal inertia peak becoming higher and the high thermal inertia peak becoming lower. Above 6 km, lower thermal inertias dominate; however, (1) the population represents only 1% of the mapped surface and (2) the lowest thermal inertias occur at much lower elevations (−4 to 2 km). At the highest elevations lower values of thermal inertia are not surprising since lower atmospheric pressure would (1) reduce the thermal conductivity (e.g., Wechsler and Glaser 1965, Jakosky 1986, Bridges 1994, Presley and Christensen 1997) and (2) cause the fine dust settling out of the atmosphere to remain trapped at the surface (e.g., Zimbelman and Kieffer 1979, Christensen 1986).

Figure 8B shows the frequency of units A, B, and C from Fig. 7 as a function of elevation. Each unit occurs at all elevations between about −4 and 6 km, where the majority of the surface is represented. Units B and C are abundant below −4 km. At the higher elevations between about 0 and 4 km, and again at the lowest elevations around −5 km, unit B tends to dominate the areal coverage. A large population of unit C occurs at lower elevations from −5 to −1 km. Units B and C combined tend to track the general distribution of elevations for the mapped locations. Unit A seems to be evenly distributed over most elevations, which would suggests relative concentration near −1 km. Unit A is also virtually absent at the lowest elevations.

If unit C represents an indurated surface, the distribution with elevation suggests that atmospheric processes may influence its formation. The occurrence of both units B and C at lower elevations initially suggests a possible genetic relation between these units, where induration is more efficient at lower elevation. However, cementing of high-thermal-inertia unit-B material to form unit-C material should raise the thermal inertia, inconsistent with the observation (see Fig. 5b). In addition, at still lower elevations unit B dominates, not unit C. It seems more plausible to suggest a genetic relationship between units A and C. Low-thermal-inertia unit-A dust could be cemented more efficiently at higher atmospheric pressures to form higher-thermal-inertia unit-C material, while darkening the surface in the process.

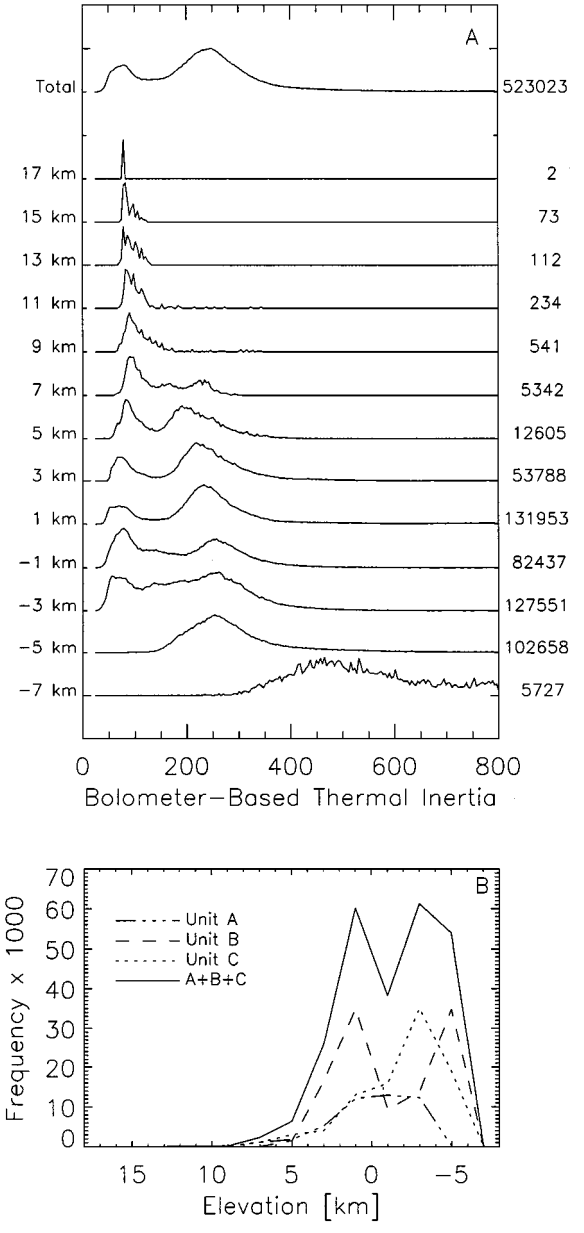

FIG. 8. (A) Correlation of elevation with thermal inertia. The right-hand list of numbers are the number of map points in each elevation bin. Bins are 2 km wide centered on the elevations listed on the left-hand side of the figure. The total histogram of thermal inertia is shown at the top for comparison. While some dependence of thermal inertia on elevation is seen at the highest and lowest elevations, intermediate elevations, where most of the planet lies, show only a weak correlation. (B) Correlation of elevation with the mapped units in Fig. 7 and Table IV. The same elevation bins are used. A clear elevation dependence is seen for the different units.

Indeed, the abundance of unit C consistently increases with decreasing elevation at the expense of unit A (see Fig. 8B). Jakosky and Christensen (1986a) suggested such a process of cementing dust to explain the relationship between Viking thermal inertia, rock abundance, and radar data. Presley and Arvidson (1988) suggested an iron sulfate cement, to both darken and redden the soil, to explain the apparent duricrust formation in eastern Oxia. The exact cementing process that forms duricrusts on Mars is as yet unknown. Certainly other explanations of Unit C are possible; to fully understand the origin and nature of this unit will require consideration of a wider range of data than is possible here.

Eolian redistribution of fines is also more efficient at higher pressures, and might also account for the lower abundance of unit A at lower elevations. In addition, if unit B were to represent a windswept surface, its presence at the lowest elevations would be consistent with particle mobility at higher atmospheric pressures, though the abundance of unit B at high elevations is inconsistent with this hypothesis.

Several smaller-scale distinct changes in the global albedo pattern have been observed in recent years by the Hubble Space Telescope (James *et al.* 1996) and by MGS (Christensen 1999). For example, the large dark albedo feature Cerberus (10°–15°N × 195°–220°W) has brightened significantly since Viking observations. Low-resolution analysis of Viking thermal inertia when Cerberus appeared dark (Palluconi and Kieffer 1981, Hayashi *et al.* 1993, Jakosky *et al.* 2000) indicates values of 200–250 and additional analysis of scattered high-resolution IRTM ground tracks indicate values of 290–380 (Zimbelman and Leshin 1987). Current TES high-resolution observations indicate a thermal inertia of 280–335 consistent with Viking high-resolution observations. The lack of a significant change in thermal inertia is supported also by Earth-based thermal infrared observation by Moersch *et al.* (1997); their results indicate that current surface temperatures are consistent with Viking-era thermal inertias. Since albedo is a measure of the top few tens of micrometers of the surface and thermal inertia is a measure of the top several centimeters, the lack of any significant change in thermal inertia for a surface that has brightened significantly indicates that Cerberus has acquired only a thin veneer of dust.

Regional Mapping and Geologic Interpretations

In this section we will examine some representative 3-km-resolution maps of thermal inertia. The intention here is not to provide a comprehensive examination of each feature presented, but to provide some examples of different features with observable signatures in thermal inertia and discuss some potential interpretations. For all the 3-km-resolution maps presented here we use nighttime bolometer-based thermal inertia.

Impact craters are abundantly visible in thermal inertia (see Fig. 2). This observation was also evident in Phobos-2 thermal inertia and thermal data (Selivanov *et al.* 1998, Betts and Murray 1993). Betts and Murray (1993) reported thermally distinct crater ejecta deposits for numerous small craters. Dark "splotch" deposits on craters floors were observed in Viking IRTM data to have thermal inertias higher than the surrounding terrains (Zimbelman and Kieffer 1979, Christensen 1983, Zimbelman 1986, Edgett and Christensen 1994). While in only a few cases were dune forms observed in images, these deposits were interpreted as intracrater dunes with particle sizes consistent with that readily transported by wind. The alignment of "splotch" deposits on the downwind side of crater interiors, relative to local wind streak patterns, supports this interpretation (e.g., Zimbelman and Kieffer 1979, Christensen 1983). Consistent with these observations, we find in the TES thermal inertia that crater floors and rims frequently exhibit higher thermal inertias than the surrounding terrain. However, not all craters exhibit a thermal inertia signature at all, suggesting that these surfaces are mantled, masking the interior, rim, and ejecta deposits. We have examined several craters reported by Betts and Murray (1993) and have not been able to confirm the presence of thermally distinct ejecta deposits in high-resolution maps; nondetection may be due to a combination of limited spatial coverage and potential miscorrelation for small craters between the MGS inertial and USGS cartographic frames.

Zimbelman (1986) examined the visible and thermal properties of the Pettit wind streak. This dark (type II) wind streak originates from a dark intracrater deposit within the 90-km crater Pettit located at about 12°N × 174°W. Viking images of the crater deposit indicate morphology consistent with dune forms (Zimbelman 1986). Figure 9A shows a TES thermal inertia map of the crater Pettit and its associated dark streak. The dark intracrater deposit has a peak thermal inertia of about 375. The streak extends to the southwest about 250 km and has thermal inertias of about 170 to 240. The surrounding terrain exhibits a low thermal inertia of about 30 to 80, indicative of unconsolidated dust (unit A in Fig. 7). If the dark high-inertia region on the crater floor is indeed dune sand that is being eroded and blown downwind, then thermal inertia can be interpreted in terms of particle size. The higher thermal inertia of the crater floor would indicate an effective particle size of 800–900 μm (Kieffer *et al.* 1973, Presley and Christensen 1997). Note that the intracrater deposit was not observed in IRTM high-resolution data, and the TES thermal inertia and interpreted particle size greatly exceeds the maximum reported by Zimbelman (1986). The reduction in thermal inertia observed downwind could indicate (1) a particle size decreasing to 100–200 μm, (2) variations in the degree of mixing of 800- to 900-μm intracrater dune sand with low-thermal-inertia dust deposits, or (3) a thin deposit of dune sand atop the low-thermal-inertia dust. Another interpretation is that saltation of intracrater dune material has eroded brighter low-thermal-inertia dust, exposing a higher-thermal-inertia rocky or indurated surface. Zimbelman (1986) showed that the rock abundances for this region were low and did not differ between the dark streak and surrounding terrain, and he favored the interpretation that the abundance of sand changes with distance from the crater source. However, exposure of an indurated surface cannot be ruled out.

Figure 9B shows a thermal inertia map of a crater near 28°S × 334°W (the largest crater right of center). In this case the entire crater floor, as well as two neighboring craters to the north and west, exhibit a high thermal inertia in excess of 480, with a peak of 760. The surrounding terrain has typical values of 220–275, including the interiors of several smaller craters. There are no apparent dark "splotch" deposits in the basemap image, as would be associated with coarse eolian material. However, the overall albedo for this region is relatively low (around 0.16–0.19) and the high thermal inertia crater floor appears slightly lighter; albedos for the Pettit wind streak are 0.2 at their lowest (Zimbelman 1986). Dark dune material could be present on the crater floor, but this would not explain the relatively low thermal inertia of the darker material outside the crater. The addition of an extensive intracrater rocky debris field, solidified impact melt or other volcanic infilling, or perhaps an extensively indurated soil localized to the crater floor might help explain these observations. Indeed, Jakosky (1986) suggested that for unconsolidated particles over about 1 mm the thermal inertias are not influenced by particle size and that higher values (thermal inertias greater than 400) may be due to induration. However, a mixture of unconsolidated coarse grains and abundant rocks and exposed bedrock might also explain the observed thermal inertia (Christensen 1986). A solid rock surface would have a thermal inertia of about 1500 to 3000, depending on composition and rock porosity. We compute thermal inertia up to a value of 800 in the present work; surfaces with temperatures consistent with a thermal inertia over 800 are present but are not mapped. It is not clear which, if any, of these or other hypotheses are more likely.

Numerous outflow channels and valleys on Mars also exhibit clear signatures in thermal inertia. Valles Marineris is large enough to begin to present a signature in Viking IRTM thermal inertia at 2° resolution (e.g., Palluconi and Kieffer 1981, Jakosky *et al.* 2000). Christensen and Kieffer (1979) mapped IRTM thermal inertias for the channeled terrains in the Chryse basin at a moderate resolution of 30 km. In general, channels floors regularly exhibit thermal inertias higher than the surrounding terrain. For example, Fig. 9C shows a large section of Kasei Vallis (near 25°N × 66°W), the largest of the catastrophic outflow channels. The correlation between the thermal inertia and the channels, channel cut walls and islands, and other flow features is striking. In addition, a clear gradation of thermal inertia is observed, increasing in the downstream direction. This trend was also observed by Christensen and Kieffer (1979), but the details are more clearly defined in the present TES data. In the context of a catastrophic flood, one might expect loose surface material to have been stripped away, exposing a high thermal inertia rock or rocky surface. On the other hand, eolian reworking and redistribution of surface material may be largely responsible for the observed thermal inertia pattern (Christensen and Kieffer 1979). Local wind streak patterns indicate westward flow that could preferentially transport atmospheric dust upstream, potentially coating surfaces. In addition, the overall thermal inertia both within and outside of the channel decreases from east to west as the surface transitions from unit C to unit A in Fig. 7 (see also Fig. 2). Clearly, many geologic processes are playing a strong roll in the development of this surface.

A thermal inertia map of Ophir Chasma is shown in Fig. 9D centered near 4°S × 72°W. The valley floor contains a variety of landslide, layered, and irregular deposits (e.g., Lucchitta *et al.* 1992). The thermal inertia pattern is complex. There is clearly higher thermal inertia within the interior of the Ophir Chasma relative to the surrounding plateau, and the canyon rim is well correlated with an increase in thermal inertia. The interior contains a full range of thermal inertia values. Several landslide deposits beneath the northern rim would likely consist of rocky debris and large blocks, but the thermal inertia is intermediate and does not reflect the boundaries of these deposits. In some areas thermal inertia boundaries seem to follow topographic features, while in other areas changes in thermal inertia seem discordant with visible features. Steep slopes, particularly along the canyon walls, may be large enough to significantly affect the thermal-inertia derivation, which assumes a horizontal surface. For example, during the northern summer (L_S around 90°) north-facing slopes will receive more direct sunlight during the day, resulting in warmer nighttime temperatures and higher apparent thermal inertias (see also Fig. 1); however, there is no obvious north–south trend in thermal inertia to correspond to this effect. It appears likely that some combination of mantling and redistribution of surface material may be strongly influencing the observed thermal inertias. Unraveling a detailed understanding of this region will be a complex task.

Figure 9E shows an eastern section of Coprates Chasma in Valles Marineris, centered at about 14°S × 59°W. The surrounding plateau has thermal inertias ranging from about 200 in the north to 300 in the south. These values are in contrast to the values of 500–800 in the canyon interior. Many locations exhibit temperatures consistent with thermal inertias higher than 800. These high thermal inertias are apparent over a large extent of Valles Marineris, as seen in Fig. 2. Within this portion of the canyon there appears to be little distinction between the wall units and the canyon floor. Again, there is no apparent difference in thermal inertia between north- and south-facing walls. Another factor that can affect the thermal inertia derivation is atmospheric dust in excess of the assumed opacity of 0.1 (normalized to 6.1 mb). While the increased column abundance due to the depth of the canyon is already included in the thermal inertia derivation, local dust concentrations can still occur. An increase in dust opacity would have the effect of increasing the apparent thermal inertia. However, dust is a transient phenomena and adjacent ground tracks represent observations taken 1 month or more apart. Excellent agreement between ground tracks suggests that transient atmospheric dust has little impact on these data. Regular nighttime haze and fog may also affect the derivation of thermal inertia by warming the surface at night, but spectral evidence for abundant water-ice clouds is absent in these observations (S. Ruff, pers. commun. 1999). If the high thermal inertia of the canyon interior represents the real character of the

surface, it is possible that this section of the canyon, including the canyon walls, is relatively windswept perhaps forming a desert pavement.

The boundary representing the transition between the three low thermal inertias regions and the surrounding terrain is fairly sharp, with an increase in thermal inertia of about 60 over a distance of several tens of kilometers (Fig. 2). If the low inertia regions do in fact represent thermally thick (greater than a few thermal skin depths), unconsolidated dust deposits, then this transition region may represent a rapid thinning of dust in a transition between unit A and unit C in Fig. 7. Figure 9F shows one of the sharper segments of this boundary near 27°N × 193°W, east of Elysium. In this case the transition from a low thermal inertia of 65 to a higher thermal inertia of 200–250 occurs over 10–30 km and in some cases over just a few kilometers, near the limit of the resolution of the TES instrument. In the middle of this map the transition is also marked by a linear ridge. The low-thermal-inertia side of this boundary has been mapped as a lower Hesperian ridged plains unit, while the higher thermal inertia side has been mapped as a lower Amazonian, Elysium Formation lava flow unit (Tanaka *et al.* 1992). Further south of this ridge the transition follows the edge of a crater ejecta deposit on the lava flow unit, but otherwise does not appear to correlate well with any mapped geologic units. In other areas within both high and low thermal inertia regions the boundaries between these same geologic units and other ridges do not correlate with thermal inertia transitions. The correlation shown in Fig. 9F could be related to material differences in the geologic units or perhaps the topography of the ridge is effecting relative dust deposition and erosion in this region. Since geologic units map large-scale morphological characteristics of the surface as seen in images, both correlation and lack of correlation with the centimeter-scale thermal layer provide some additional insights about the physical character of the surface material within mapped units.

Figure 9G shows thermal inertia units that appear to correlate with local geologic units. This map is located south of Daedalia Planum 35°S × 137°W. Higher thermal inertia regions (with values of 300–360) correlate well with a mapped Hesperian Tharsis volcanic unit, comprising relatively smooth lava flows that embay highland cratered terrain (Scott and Tanaka 1986). The surrounding lower thermal inertia regions (with values of 200–250) correspond with several Hesperian ridged plains and Noachian hilly and cratered units (Scott and Tanaka 1986). The boundary between the high and the low thermal inertia units is sharp (at the limit of TES resolution) and mostly corresponds with the boundaries between the mapped units. It is unclear what might be causing such a sharp transition and the correlation with the geologic units. One possibility is that a thermally thin deposit (much less than a thermal skin depth) mantles the entire region, covering volcanic rock in the higher thermal inertia regions and lower thermal inertia impact breccia and regolith in the low inertia regions, thus allowing the subsurface unit to effect the bulk thermal inertia. Another possibility is that small-scale roughness and rock abundance may be higher on the volcanic unit, though the relative rock abundance would need to increase by about 25% to account for the observed increase in thermal inertia (Christensen 1986).

In general, we find there to be a sporadic correlation between mapped geologic and geomorphic units and spatial variations in thermal inertia. Strong correlation occurs with flood channels where channel floors have higher thermal inertias than the surrounding surface. Many impact crater rims and floors tend to exhibit some signature with the strongest correlation with dark crater floor deposits, which are probably coarse sand dune deposits. In contrast, there are numerous craters that do not exhibit any thermal inertia signature, suggesting that these surfaces are mantled. Any lack of correlation with geologic units is not surprising, since these units tend more to map features tens of meters or larger in scale than are visible in orbiter images. Thermal inertia is sensitive to the top few centimeters of the surface. Mantling of the surface by a few-centimeter-thick layer can alter the thermal signature without noticeably affecting the geomorphic signature. Finding geologic correlations would imply either that thermal inertia is sensing the bedrock geology in these regions or that the geology is somehow controlling the overlying thermal layer. Aeolian reworking of the surface would be dominated by large-scale wind patterns which are topographically controlled. Although mechanisms for indurating the surface are still debated, topography and bedrock chemistry might be controlling factors.

Mapping the thermal inertia of the martian surface at 3 km resolution reveals a great deal of detail that was previously unseen. Correlations and noncorrelations with the underlying geology and specific geomorphic features is providing new insights and raising new questions about the nature of the martian surface. Lower resolution IRTM mapping blends together the nonlinear effects of high and low thermal inertia surfaces into an effective inertia for a single large footprint. The present 3-km-resolution data separates these subpixel inhomogeneities and presents a wider range of thermal inertia values.

SUMMARY

We present new maps of high-resolution thermal inertia derived from surface temperature observations from the Mars Global Surveyor Thermal Emission Spectrometer, obtained during the beginning of the mapping mission. Thermal inertias are derived from single-temperature observations from the TES thermal bolometer and infrared spectrometer. The method employs a state-of-the-art thermal model to generate a seven dimensional lookup table which is interpolated for each TES observation. Nighttime thermal inertias are presented. Comparisons between TES thermal inertia and Viking-era low-resolution thermal inertia and between bolometric and spectral 20-μm thermal inertia suggest that this method works well. Formal uncertainties are estimated to be around 6% for the bolometric

thermal inertia and around 16.9% for the spectrometer-based thermal inertia; however, comparisons and analysis suggest the actual uncertainties are much lower.

Global correlation between the TES bolometric thermal inertia and TES albedo shows a clear trimodal behavior. In addition to the two high-thermal-inertia/low-albedo and low-thermal-inertia/high-albedo modes present in the Viking IRTM thermal inertia analysis, a new third mode of moderate-to-high thermal inertia and an intermediate albedo is observed. Better quality and resolution of both thermal inertia and albedo allow this mode to be discerned. Along with the presences of a broad high thermal-inertia mode in the Viking analysis, these results suggest that the third mode does not represent a change in the surface of Mars, but rather an improved observation. This third mode (unit C in Fig. 7) maps a distinct surface unit, with significant areal coverage, that surrounds the low thermal inertia regions. This unit is more abundant at lower elevations. Both Viking landing sites map onto unit C, while the Pathfinder landing site exhibits higher thermal inertia. Duricrust and indurated soil material has been observed at all the landing sites and may represent this unit. Correlation of unit C with several earlier studies mapping regions of potentially indurated soil supports this hypothesis. The generally low elevation of unit C suggests that atmospheric processes may play a role in the formation of this unit. We favor a possible genetic relation where low thermal inertia regions transition to unit C by induration. In general, a better understanding of geologic and physical characteristics of the high-thermal-inertia/low-albedo and low-thermal-inertia/high-albedo (units B and A in Fig. 7, respectively) and their relationship to unit C would be greatly extended by landed missions to regions on these surface units.

High-resolution thermal inertia mapping has been performed for several localized areas. Many impact crater rims and intracrater dunes show higher thermal inertias than the surrounding terrain. In contrast, there are many impact craters that do not exhibit any thermal inertia signature, which suggest postimpact mantling of the surface in these regions. The thermal inertia of intracrater dune deposits and wind streaks can be related to average particle size for a loose windblown material. Outflow channels consistently show higher thermal inertias than the surrounding terrain; the lower elevation and higher atmospheric pressure at the channel floor may be responsible for trapping deposits of larger particles, or in extreme cases leaving the surfaces windswept, forming a high thermal inertia desert pavement. Mapped geologic units sometime correlate with spatial variations in thermal inertia, suggesting some relationship between the tens to hundreds of meter-scale morphology and the centimeter-scale thermal layer in these regions. Generally, at the present 3-km resolution, spatial variations in thermal inertia tends to reflect the local geomorphology, though for many areas there is no correlation. While the former may be the most informative about geologic processes, the latter may be the most intriguing.

FUTURE RESEARCH

Thermal inertia mapping will continue during the course of the MGS mission. Greater spatial coverage and greater latitudinal extent is expected. We plan to improve the quality of thermal inertia values by incorporating spatially and temporally variable dust opacities and by including the highest quality albedo and elevation maps into the processing as they become available. Thermal inertias will be available through the Planetary Data System.

ACKNOWLEDGMENTS

We thank the numerous people responsible for the success of the MSG mission and the quality data produced by the TES instrument. We are grateful to Michael Smith for providing dust opacity information from TES observations and Steve Ruff for helpful discussions on the spectral characteristics of the surface. We thank Frank Palluconi and Ken Edgett for constructive reviews. We also thank Shannon Pelkey and Noel Gorelick for assistance in producing high-resolutions maps. This work was supported in part by the Mars Global Surveyor Science Office (B.M.J. as Interdisciplinary Scientist; P.R.C. and H.H.K. as TES Science Team members).

REFERENCES

Arvidson, R. E., E. A. Guinness, M. A. Dale-Bannister, J. Adams, M. Smith, P. R. Christensen, and R. B. Singer 1989. Nature and distribution of surficial deposits in Chryse Planitia and vicinity, Mars. *J. Geophys. Res.* **94**, 1573–1587.

Betts, B. H., and B. C. Murray 1993. Thermally distinct ejecta blankets from martian craters. *J. Geophys. Res.* **98**, 11,043–11,059.

Betts, B. H., B. C. Murray, and T. Svitek 1995. Thermal inertias in the upper millimeter of the martian surface derived using Phobos' shadow. *J. Geophys. Res.* **100**, 5285–5296.

Binder, A. B., R. E. Arvidson, E. A. Guinness, K. L. Jones, E. C. Morris, T. A. Mutch, D. C. Pieri, and C. Sagan 1977. The geology of the Viking Lander 1 site. *J. Geophys. Res.* **82**, 4439–4451.

Bridges, N. T. 1994. Elevation-corrected thermal inertia and derived particle size on Mars and implications for the Tharsis Montes. *Geophys. Res. Lett.* **21**, 785–788.

Christensen, P. R. 1982. Martian dust mantling and surface composition: Interpretation of thermophysical properties. *J. Geophys. Res.* **87**, 9985–9998.

Christensen, P. R. 1983. Eolian intracrater deposits on Mars: Physical properties and global distribution. *Icarus* **56**, 496–518.

Christensen, P. R. 1986. The spatial distribution of rocks on Mars. *Icarus* **68**, 217–238.

Christensen, P. R., and H. H. Kieffer 1979. Moderate resolution mapping of Mars: The channel terrain around the Chryse basin. *J. Geophys. Res.* **84**, 8233–8238.

Christensen, P. R., and M. C. Malin 1988. High resolution thermal imaging of Mars. *Proc. Lunar Planet. Sci. Conf. 19th*, 180–181.

Christensen, P. R. 1999. Global view of surface materials, In *The Fifth International Conference on Mars*, Lunar Planet. Inst. Contribution 972, Pasadena.

Christensen, P. R., and H. J. Moore 1992. The martian surface layer. In *Mars* (H. H. Kieffer, B. M. Jakosky, C. W. Snyder, and M. S. Matthews, Eds.). Univ. Arizona Press, Tucson.

Christensen, P. R., D. L. Anderson, S. C. Chase, R. N. Clark, H. H. Kieffer, M. C. Malin, J. C. Pearl, J. Carpenter, N. Bandiera, F. G. Brown, and S.

Silverman 1992. Thermal emission spectrometer experiment: Mars Observer. *J. Geophys. Res.* **97**, 7719–7734.

Clark, B. C., A. K. Baird, R. J. Weldon, D. M. Tsusaki, L. Schnabel, and M. P. Candelaria 1982. Chemical composition of martian fines. *J. Geophys. Res.* **87**, 10,059–10,067.

Ditteon, R. 1982. Daily temperature variations on Mars. *J. Geophys. Res.* **87**, 10,197–10,214.

Edgett, K. S., and P. R. Christensen 1994. Mars aeolian sand: Regional variations among dark-hued crater floor features. *J. Geophys. Res.* **99**, 1997–2018.

Golombek, M. P., H. J. Moore, A. F. C. Haldemann, T. J. Parker, and J. T. Schofield 1999. *J. Geophys. Res.* **104**, 8585–8594.

Haberle, R. M., and B. M. Jakosky 1991. Atmospheric effects on the remote determination of thermal inertia on Mars. *Icarus* **90**, 187–204.

Hayashi, J. N., B. M. Jakosky, and R. M. Haberle 1995. Atmospheric effects on the mapping of martian thermal inertia and thermally derived albedo. *J. Geophys. Res.* **100**, 5277–5284.

Jakosky, B. M. 1979. The effects of nonideal surfaces on the derived thermal properties of Mars. *J. Geophys. Res.* **84**, 8252–8262.

Jakosky, B. M. 1986. On the thermal properties of martian fines. *Icarus* **66**, 117–124.

Jakosky, B. M., and P. R. Christensen 1986a. Global duricrust on Mars: Analysis of remote-sensing data. *J. Geophys. Res.* **91**, 3547–3559.

Jakosky, B. M., and P. R. Christensen 1986b. Are the Viking Lander sites representative of the surface of Mars? *Icarus* **66**, 125–133.

Jakosky, B. M., M. T. Mellon, H. H. Kieffer, P. R. Christensen, E. S. Varnes, and S. W. Lee 2000. The thermal inertia of Mars from the Mars Global Surveyor Thermal emission spectrometer. *J. Geophys. Res.* **105**, 9643–9652.

James, P. B., J. F. Bell, R. T. Clancy, S. W. Lee, L. J. Martin, and M. Wolff 1996. Global mapping of Mars by Hubble Space Telescope during the 1995 opposition. *J. Geophys. Res.* **101**, 18,883–18,890.

Kieffer, H. H. 1976. Soil and surface temperatures at the Viking landing sites. *Science* **194**, 1344–1346.

Kieffer, H. H., S. C. Chase, E. Miner, G. Münch, and G. Neugebauer 1973. Preliminary report on infrared radiometric measurements from the Mariner 9 spacecraft. *J. Geophys. Res.* **78**, 4291–4312.

Kieffer, H. H., T. Z. Martin, A. R. Peterfreund, B. M. Jakosky, E. D. Miner, and F. D. Palluconi 1977. Thermal and albedo mapping of Mars during the Viking primary mission. *J. Geophys. Res.* **82**, 4249–4291.

Ksanfomaliti, L. V., and V. I. Moroz 1975. Infrared radiometry on board Mars-5. *Cosmic Res.* **13**, 65–67.

Leovy, C. 1966. Note on thermal properties of Mars. *Icarus* **5**, 1–6.

Lucchitta, B. K., A. S. McEwen, G. D. Clow, P. E. Geissler, R. B. Singer, R. A. Shultz, and S. W. Sqyures 1992. The canyon system on Mars. In *Mars* (H. H. Kieffer, B. M. Jakosky, C. W. Snyder, and M. S. Matthews, Eds.). Univ. of Arizona Press, Tucson.

Merényi, E., K. S. Edgett, and R. B. Singer 1996. Deucalionis Regio, Mars: Evidence for a new type of immobile weathered soil unit. *Icarus* **124**, 296–307.

Moersch, J. E., J. F. Bell, L. Carter, T. Hayward, P. Nicholson, S. Squyres, and J. Van Cleve 1997. What happened to Cerberus? Telescopically observed thermophysical properties of the martian surface. Mars Telescopic Observations Workshop II, Tucson, L.P.I. Tech. Rep. 97-03.

Moore, H. J., D. B. Bickler, J. A. Crisp, H. J. Eisen, J. A. Gensler, A. F. C. Haldemann, J. R. Matijevic, L. K. Reid, and F. Pavlics 1999. Soil-like deposits observed by Sojourner, the Pathfinder rover. *J. Geophys. Res.* **104**, 8729–8746.

Moroz, V. I., and L. V. Ksanfomaliti 1972. Preliminary results of astrophysical observations of Mars from Mars-3. *Icarus* **17**, 408–422.

Moroz, V. I., L. V. Ksanfomaliti, G. N. Krasovskii, V. D. Davydov, N. A. Parfentèv, V. S. Zhengulëv, and G. F. Filippov 1976. Infrared temperatures and thermal properties of the martian surface measured by the Mars 3 Orbiter. *Cosmic Res.* **13**, 346–356.

Morrison, D., C. Sagan, and J. B. Pollack 1969. Martian temperatures and thermal properties. *Icarus* **11**, 36–45.

Mutch, T. A., R. E. Arvidson, A. B. Binder, E. A. Guinness, and E. C. Morris 1977. The geology of the Viking Lander 2 site. *J. Geophys. Res.* **82**, 4452–4467.

Neugebauer, G., G. Münch, H. Kieffer, S. C. Chase, and E. Miner 1971. Mariner 1969 infrared radiometer results: Temperatures and thermal properties of the martian surface. *Astron. J.* **76**, 719–728.

Paige, D. A., and K. D. Keegan 1994. Thermal and albedo mapping of the polar regions of Mars using Viking thermal mapper observations 1. South polar region. *J. Geophys. Res.* **99**, 25,992–26,013.

Paige, D. A., J. E. Bachman, K. D. Keegan 1994. Thermal and albedo mapping of the polar regions of Mars using Viking thermal mapper observations. 1. North polar region. *J. Geophys. Res.* **99**, 25,959–25,991.

Palluconi, F. D., and H. H. Kieffer 1981. Thermal inertia mapping of Mars from 60°S to 60°N. *Icarus* **45**, 415–426.

Pleskot, L. K., and E. D. Miner 1981. Time variability of martian bolometric albedo. *Icarus* **45**, 179–201.

Pollack, J. B., R. M. Haberle, J. Schaffer, and H. Lee 1990. Simulations of the general circulation of the martian atmosphere. 1. Polar processes. *J. Geophys. Res.* **95**, 1447–1473.

Presley, M. A., and R. E. Arvidson 1988. Nature and origin of materials exposed in Oxia Palus—Western Arabia—Sinus Meridiani Region of Mars. *Icarus* **75**, 499–517.

Presley, M. A., and P. R. Christensen 1997. Thermal conductivity measurements of particulate materials. 2. Results. *J. Geophys. Res.* **102**, 6551–6566.

Scott, D. H., and K. L. Tanaka 1986. *Geologic Map of the Western Equatorial Region of Mars*. U.S. Geological Survey, Map I-1802-A.

Selivanov, A. S., Yu. M. Gektin, N. K. Naraeva, R. O. Kuzmin, Yu. S. Tyuflin, T. Duxbury, and V. I. Moroz 1998. *Atlas of Mars by the TERMOSCAN Radiometer Data*. Assoc. Adv. Space Sci. Tech. Moscow.

Sinton, W. M., and J. Strong 1960. Radiometric observations of Mars. *Astrophys. J.* **131**, 459–469.

Smith, D., M. Zuber, S. Solomon, R. Phillips, J. Head, J Garvin, W. Banerdt, D. Muhleman, G. Pettengill, G. Neumann, F. Lemoine, J. Abshire, O. Aharonson, C. Brown, S. Hauck, A. Ivanov, P. McGovern, H. Zwally, and T. Duxbury 1999. The global topography of Mars and implications for surface evolution. *Science* **284**, 1495–1503.

Tanaka, K. L., M. G. Chapman, and D. H. Scott 1992. *Geologic Map of the Elysium Region of Mars*. U.S. Geological Survey, Map I-2147.

Tillman, J. E., N. C. Johnson, P. Guttorp, and D. B. Percival 1993. The martian annual atmospheric pressure cycle: Years without great dust storms. *J. Geophys. Res.* **98**, 10,963–10,971.

Wechsler, A. E., and P. E. Glaser 1965. Pressure effects on postulated lunar materials. *Icarus* **4**, 335–352.

Zimbelman, J. R. 1986. Surface properties of the Pettit wind streak on Mars: Implications for sediment transport. *Icarus* **66**, 83–93.

Zimbelman, J. R., and H. H. Kieffer 1979. Thermal mapping of the northern equatorial and temperate latitudes of Mars. *J. Geophys. Res.* **84**, 8239–8251.

Zimbelman, J. R., and L. A. Leshin 1987. A geologic evaluation of thermal properties for the Elysium and Aeolis Quadrangles of Mars. *J. Geophys. Res.* **92**, E588–E596.